MnO$_x$-Electrodeposited Fabric-Based Stretchable Supercapacitors with Intrinsic Strain Sensing

Abhilash Pullanchiyodan, Libu Manjakkal, Markellos Ntagios, and Ravinder Dahiya*

ACCESS | Metrics & More | Article Recommendations | Supporting Information

ABSTRACT: The increasing number of devices needed by wearable systems to bring radical advances in healthcare, robotics, and human−machine interfaces is a threat to their growth if the integration and energy-related challenges are not managed. A natural solution is to reduce the number of devices while retaining the functionality or simply using multifunctional devices, as demonstrated here through a stretchable supercapacitor (SSC) with intrinsic strain sensing. The presented SSC was obtained by electrodeposition of nanoflower MnO$_x$ on fabric (as a pseudocapacitive electrode) and three-dimensional conductive wrapping of poly(3,4-ethylenedioxythiophene):poly(styrene sulfonate) (PEDOT:PSS) to boost the performance. Among fabricated devices, the stretchable PEDOT:PSS/MnO$_x$/PEDOT:PSS supercapacitor (SPMP-SC) showed the best performance (specific capacitance of 580 mF·cm^{-2} (108.1 F·g^{-1}); energy density of 51.4 μWh·cm^{-2} at 0.5 mA). The stretchability (0−100%; 1000 cycles) analysis of SPMP-SC with Ecoflex encapsulation showed high capacitance retention (>90% for 40% stretch). The intrinsic strain sensing of the SSC was confirmed by the linear variation of capacitance (sensitivity −0.4%) during stretching. Finally, as a proof-of-concept, the application of SSC with intrinsic sensing was demonstrated for health monitoring through volumetric expansion of a manikin during ventilator operation and in robotics and by measuring the joint angle of a robotic hand.

KEYWORDS: stretchable supercapacitors, manganese oxides, strain sensors, multifunctional supercapacitors, intrinsic sensing
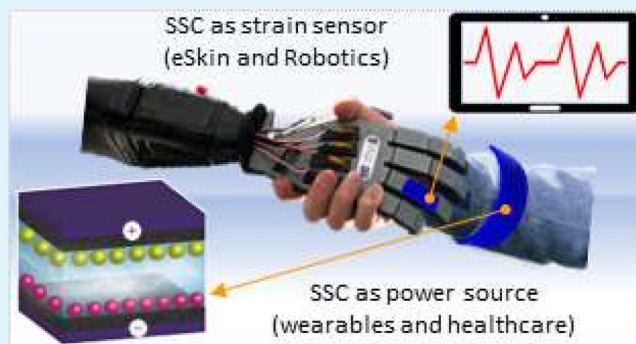
1. INTRODUCTION

The advancements in wearable electronics and the rapid increase in the number of sensors and electronic devices they use to meet the requirements of popular applications such as health monitoring,[1,2] electronic skins,[3,4] robotics,[5] implantable devices,[6,7] flexible displays,[8] and wearable sensors[9−11] have brought to the fore the need for compatible energy storage devices (e.g., batteries and supercapacitors (SCs)). The energy storage devices in these applications are expected to deliver consistent power under mechanical deformations such as bending, twisting, and stretching,[12−16] which could also lead to variations in the electrode−electrolyte interactions and hence the performance of the energy storage devices. Such intrinsic variations in the performance of these devices turned out to be attractive as they open an interesting opportunity for using them as sensors, in addition to their typical use as energy storage devices. Material integrated sensing or the intrinsic sensing of energy storage devices can be hugely beneficial for applications such as wearable systems where the ever-increasing number of single-functionality devices is detrimental to user acceptance as it comes at the cost of comfort.[17,18] Likewise, in applications such as eSkin for robotics, such multifunctional devices could immensely help by lowering the

number of sensors without sacrificing the richness of gathered data and at the same time reducing the overall weight of eSkin.[18] Recently, the intrinsic sensing of devices such as solar cells (as touch sensors, in addition to energy generation[19]), coil-based actuators (also used as touch sensors[20]), antenna (as a temperature sensor, in addition to wireless data transmission[21]), and flexible SCs (as mechanical strain sensors)[22,23] has been reported. However, the multifunctional use of energy storage devices has not been explored. Herein, with a binary redox state of MnO$_x$-based stretchable supercapacitors (SSCs) (580 mF·cm^{-2} (108.1 F·g^{-1}) capacitance, 51.4 μWh·cm^{-2} energy density, and high capacitance retention on stretching), we demonstrate for the first time the dual-function (energy storage and self-powered strain sensors) SCs.

The material selection and design play a vital role in attaining sufficient stretchability and acceptable multifunc-

tional performance of SSCs[11] such as liquid metals.[24,25] In this regard, textile-based electrodes are considered the most suitable owing to their porous nature, good stretchability, low cost, and ease of functionalization.[11,15,26] However, the poor energy density of textile-based SSCs has been a factor that limits their wider use,[27] and the issue is commonly addressed by depositing on the textile pseudocapacitive materials such as manganese oxides (MnO_2 and Mn_3O_4) and ruthenium oxide (RuO_2).[11,28,29] MnO_2 is particularly attractive due to its better theoretical specific capacitance (1300 F/g), low cost, and abundant availability in nature.[30−36] Recently, Mn_3O_4 has also gained some interest in SCs due to the coexistence of Mn^{2+} and Mn^{3+}, which provide more ions in pseudocapacitance generation.[37] Different types of Mn_3O_4 nanostructures doped with other ions have been shown to exhibit excellent capacitance performance.[38−42] The latest developments illustrate that the binary combination of redox states of these oxides (Mn_3O_4 and MnO_2) may offer a potentially better solution for the electrode of the SCs.[43] This is because the synergistic contribution from both redox states of this oxide increases the capacitance of the electrode material compared to their individual use.[43] As a result, the active electrodes of the new SSC presented here are based on the binary redox states of MnO_x, and their performance is further improved by three-dimensional (3D) wrapping with a conductive polymer network. The 3D wrapping technique is a new way to boost the performance of SCs and overcomes previous challenges due to the low electron transport of pseudocapacitive materials.[44] Furthermore, the 3D wrapping with a conducting polymer could reduce the strain-induced degradation of MnO_2 capacitance due to its intrinsic rigid structure. As a result, the capacitance tolerance of the SSC is enhanced and the multifunctionality of the device is supported.[45]

The poor performance and shorter life of SCs as a result of the low electrical conductivity (10^{-5} to 10^{-6} S/cm),[46] low ionic diffusion constant ($\sim 10-13$ $cm^2/(V\ s)$),[46] and dissolution of MnO_2[34,35,47−49] could be improved by 3D wrapping of these metal oxides with different conducting materials such as carbon nanotubes, graphene, polyaniline, polypyrrole, and poly(3,4-ethylenedioxythiophene):poly-(styrene sulfonate) (PEDOT:PSS).[49−55] This type of wrapping could enhance the connectivity between the nanoparticles and thus increase the ionic/electronic conductivity. Furthermore, the wrapped conductive materials offer an additional conductive network, which contributes to the total capacitance of the SC through the formation of an electric double-layer capacitance (edlc). Among various conductive wrapping materials to improve the performance of the MnO_2 electrode, the PEDOT:PSS has an edge as it provides better interconnectivity (conductivity) and intertwines (bonding) even in low-surface-area conditions.[44,49] The enhanced interconnectivity due to 3D wrapping helps attain better performance even under stretching conditions. Additionally, we observed a direct relation of the capacitance variation of the SSC with applied mechanical strain, which opens a new route for their multifunctional use. This sets off new applications for SCs, specifically for SSCs, as energy storage devices with intrinsic strain sensing. The high cyclic stability and linear variation of capacitance of the presented SSCs with stretching prove their suitability as strain sensors for various applications as demonstrated through powering an LED and volumetric expansion/contraction of the chest. Such devices could find potential applications in wearables for health monitoring, for example, during the current pandemic situation.

2. EXPERIMENTAL SECTION

2.1. Materials and Methods. In this work, we used a plain lycra fabric (nylon and spandex mix) as a stretchable substrate for SC fabrication. To convert the nonconducting fabric to conductive, it was coated with a PEDOT:PSS solution doped with 5 wt % DMSO. Prior to coating, the fabric was first washed with acetone and then with sodium hydroxide (NaOH, 1 M) solution at 80 °C for 1 h, followed by distilled water and then dried at 80 °C for 2 h. The coating was then carried out on the dried fabric by the drop-casting technique, and the fabric was allowed to dry at the same condition in a hot-air oven. MnO_x was deposited on this conductive fabric through electrochemical deposition using a workstation (Metrohm Autolab, PGSTAT302N). The electrolyte for the deposition was prepared by dissolving manganese acetate (0.1 M) in distilled water. In a typical deposition process, PEDOT:PSS-coated fabric (3 cm^2 area) was used as the working electrode, Ag/AgCl as the reference electrode, and platinum wire as the counter electrode (shown in Figure S1). The deposition was carried out by the chronoamperometric technique with an applied potential of 1.5 V for 30 min. Finally, the deposited film on the fabric was washed with distilled water to remove the excess electrolytic impurities and dried at 80 °C for 2 h. For conductive wrapping, the MnO_x-deposited fabrics were further drop-cast with PEDOT:PSS-5% DMSO solution and subjected to the same drying procedure as before.

2.2. Electrolyte Preparation and SC Assembly. Poly(vinyl alcohol) (PVA)-potassium chloride (KCl) gel electrolyte was used for SC fabrication as it is a safe and biocompatible electrolyte. The gel electrolyte was prepared based on our previous report by dissolving 10% PVA in water under heating at 85 °C for 1 h followed by the addition of the aqueous KCl solution.[13] A stretchable cloth (mentioned in Section 2) having an active area of 3 cm^2 was used as the electrode for fabricating SP-SC (stretchable PEDOT:PSS-based supercapacitor), SPM-SC (stretchable PEDOT:PSS/MnO_x-based supercapacitor), and SPMP-SC (stretchable PEDOT:PSS/MnO_x/ PEDOT:PSS-based supercapacitor). For external connection, a wire was fixed on top of the conducting fabric using silver (Ag) conductive epoxy (from RS components, 186-3600). For stretchable studies, Ecoflex 00-30 (50:50 ratio of parts A and B) was used as the stretchable encapsulation material.

2.3. Characterizations. The phase and structural analyses of the PEDOT:PSS-coated and MnO_x-deposited fabrics were carried out using an X-ray diffractometer (XRD, P'Analytical X'Pert with Cu Kα (λ = 1.541 Å)). The corresponding peaks were identified and indexed using standard JCPDS files (75-1560 for Mn_3O_4 and 44-0992 for MnO_2). The microstructural analysis was carried out by a scanning electron microscope, SEM (FEI Nova). The electrochemical analysis, including CV (1−200 mV·s^{-1}) and EIS (1 mHz to 1 MHz, in a potential amplitude of 10 mV), was performed using an electrochemical workstation (Metrohm Autolab, PGSTAT302N) with a two-electrode system. The GCD analysis was carried out with a source meter (Agilent, U2722A) controlled through the LabVIEW program at different applied current densities. The variation in the capacitance with static and dynamic stretching was measured from CV and GCD analyses by stretching (strain) the SCs with a step-controlled Pollux motor system from 0 to 100%.

2.4. Demonstration of Dual Functions of SSC. For dual-function (i.e., as strain sensor and energy storage) testing of SSC, an array of SPMP-SCs (three devices in series) with Ecoflex encapsulation was fabricated and fixed on the chest of a manikin connected with a DIY ventilator. The ventilator uses a manual resuscitator Ambu bag to provide the air to the manikin's artificial lungs. The bag is deformed under the forces of two pistons that are moving toward it and are mechanically coupled with a stepper motor. The system can be powered either with Li-ion batteries or via a 9 V DC supply. The breaths per minute can be set from a potentiometer.[56] The capacitance variation of the SSC during the
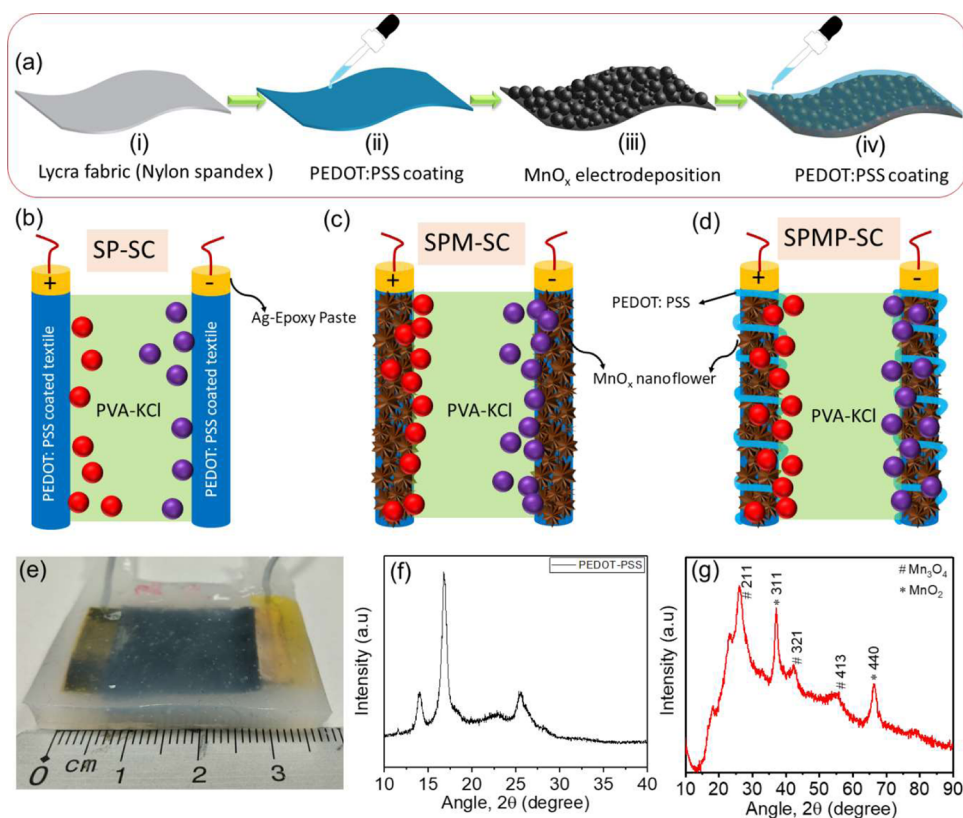
Figure 1. (a) Fabrication steps for the SSC electrodes, and schematic representation of (b) SP-SC, (c) SPM-SC, and (d) SPMP-SC. (e) Image of the SPMP-SC encapsulated in Ecoflex. (f) and (g) XRD patterns of PEDOT:PSS and MnO_x films, respectively.

ventilation was measured using an LCR meter interfaced by the LABVIEW program. To test the powering ability of the SSC during the ventilation, the SSC array was connected to an LED and the lighting condition was monitored with stretching.

3. RESULTS AND DISCUSSION

3.1. Stretchable Electrode for SC Fabrication. Figure 1a shows the fabrication steps for SSC electrodes (details provided in the Experimental section). The electrodes were fabricated on a stretchable lycra fabric (step i) coated with a PEDOT:PSS conducting polymer (step ii) followed by electrodeposition of MnO_x active material (step iii) (a short description of the electrodeposition and its schematic representation is given in Figure S1 in the Supporting Information). For enhanced conductivity and to improve the performance of the SSC, the 3D or all-around wrapping of MnO_x nanoparticles with the PEDOT:PSS polymer was carried out in step iv. Using these electrodes, we fabricated three types of SSCs to investigate the role played by each of the above components toward the final performance. Figure 1b−d shows the schematic illustration of these symmetric SSCs. The SP-SC uses PEDOT:PSS-coated lycra fabric as the electrode (Figure 1b), whereas the electrodes of SPM-SC contain MnO_x over the PEDOT:PSS-coated fabrics (Figure 1c). Likewise, the SPMP-SC has an electrode based on PEDOT:PSS wrapped (3D conductive) on the MnO_x-deposited conductive (PEDOT:PSS-coated) fabric (Figure 1d). The Ecoflex was used as an encapsulant for these SSCs, as shown in the image of the final SPMP-SC in Figure 1e.

3.2. Structural and Morphological Characterization of Electrodes. The structural analysis of the fabric electrodes was carried out using an X-ray diffractometer (XRD). Figure 1f

shows the XRD pattern of the PEDOT:PSS-coated fabric at diffraction angles of 10−40°. Among the three main peaks in Figure 1f, the broad peak at $2\theta \sim 26°$ arises from the $\pi-\pi$ stacking of the thiophene ring in PEDOT, whereas the peak at $2\theta \sim 14°$ originates from the second-order lamellar stacking of the PEDOT:PSS chain. The peak at $2\theta \sim 17°$ is from the PSS chains present in the material. The coexistence of Mn_3O_4 and MnO_2 phases of the electrodeposited MnO_x film was confirmed by the XRD pattern in Figure 1g.

The microstructural analysis of the bare and functionalized (PEDOT:PSS-coated, MnO_x-deposited, and 3D-wrapped) fabrics was carried out with a scanning electron microscope (SEM), and the results are shown in Figure 2. The optical (photographic) image of the bare fabric is given in Figure 2a. The SEM images in Figure 2b,c show a bundle of fibers having a uniform microstructure. As shown in Figure 1a in step ii, the PEDOT:PSS ink was coated on this fabric and its uniform distribution is visible from the optical image shown in Figure 2d (blue color). The presence of the polymer layer on each thread of the stretchable fabric indicates a uniform coating, and it was also observed from the magnified SEM images given in Figure 2e,f. The microstructures of electrodeposited MnO_x (Mn_3O_4/MnO_2) on this conducting fabric are shown in Figure 2g−i. The black color on the fabric, as evident from the photograph shown in Figure 2g, indicates the uniform deposition of manganese oxide. From the SEM image (Figure 2h,i), it is evident that the MnO_x forms a porous nanoflower (NF)-like morphology with a bunch of nanopetals. Such a porous NF structure is desirable as it improves the specific surface area and hence the capacitance of SC.[38,57,58] The porous structure is also desirable because the electrochemical performance of pseudocapacitive materials depends on its
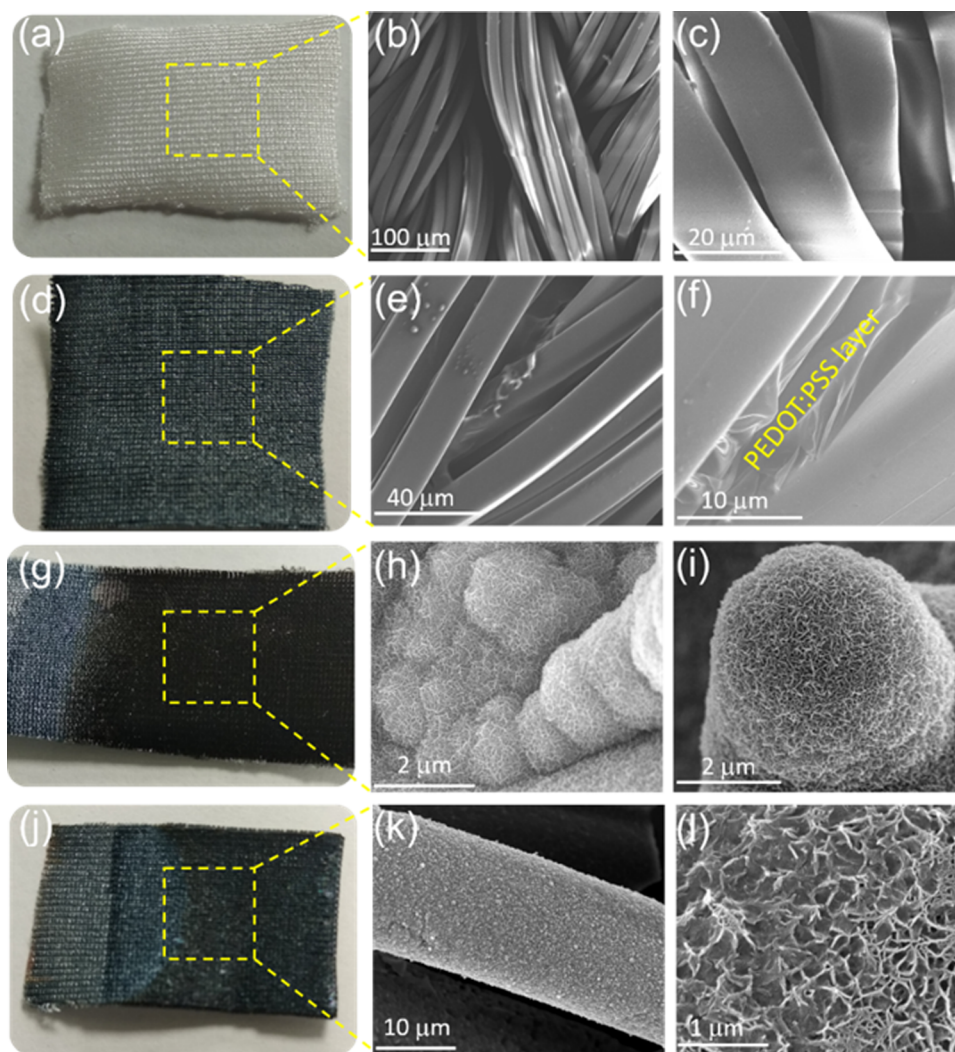
Figure 2. Digital and SEM images of the bare lycra fabric (a−c), PEDOT:PSS-coated fabric (d−f), MnO_x electrodeposited on PEDOT:PSS-coated fabric (g−i), and PEDOT:PSS 3D-wrapped on MnO_x-electrodeposited fabric (j−l).

morphology, porosity, surface area, and ionic transport within these pores.[50] To further enhance the electrical conductivity of deposited MnO_x, a 3D conductive wrapping was carried out with drop-casting of a PEDOT:PSS-5 wt % dimethyl sulfoxide (DMSO) solution on the MnO_x-deposited fabric. The photograph of the 3D conductive wrapped electrode is shown in Figure 2j, and the microstructures are shown in Figure 2k,l. A closer analysis of microstructures reveals that the deposited MnO_x NFs are well interconnected with the PEDOT:PSS polymer chain and maintain the porous structure. Here, the rationale behind selecting PEDOT:PSS for conductive wrapping is that as a water-soluble polymer it can make a better interconnection with the underlying MnO_x layer and thereby improve the electrochemical access and the performance.

3.3. Electrochemical Analysis of the SSC. The electrochemical impedance spectroscopic (EIS) analysis of the SCs was carried out in the frequency range of 1 mHz to 1 MHz, and the results are shown in Figure 3a,c and in Figure S2 (Bode plot) in the Supporting Information. Figure 3a shows a comparison of the Nyquist plot of the fabricated SSCs, with the behavior in the high-frequency region shown in the inset. The solution resistance (R_s) values (measured at the point of intercept at high frequency) due to the electrode−electrolyte

interaction of SP-SC, SPM-SC, and SPMP-SC were 44, 57, and 48 Ω, respectively. The results show that the electrodeposition of MnO_x increases the value of R_s, possibly due to the nonconducting behavior of this metal oxide. Nonetheless, this was reduced to 48 Ω by wrapping of the conductive PEDOT:PSS layer (SPMP-SC). Similarly, we observed a change in the diameter of the semicircle in the Nyquist plot, which relates to the charge-transfer resistance (R_{ct}) due to the porous electrode material reaction with ions in the KCl gel electrolyte. As shown in the inset of Figure 3a, the SPMP-SC shows the lowest diameter and a sharp vertical line in the low-frequency range as compared to the plots for SP-SC and SPM-SC. These results confirm the role of PEDOT:PSS 3D wrapping on MnO_x nanoparticles, which is to reduce the internal resistance and to improve interparticle conductivity for ionic diffusion.

To obtain an insight into the mechanism and contribution of each parameter on the total capacitance and resistance of the devices, we carried out electrochemical fitting analysis of the Nyquist plot of each device (shown in Figure 3b for SPMP-SC, Figure S3a for SP-SC, and Figure S3b for SPM-SC in the Supporting Information). The circuit used for fitting is a typical Randles circuit with secondary diffusion and is given in the inset of each figure. The obtained parameters after fitting
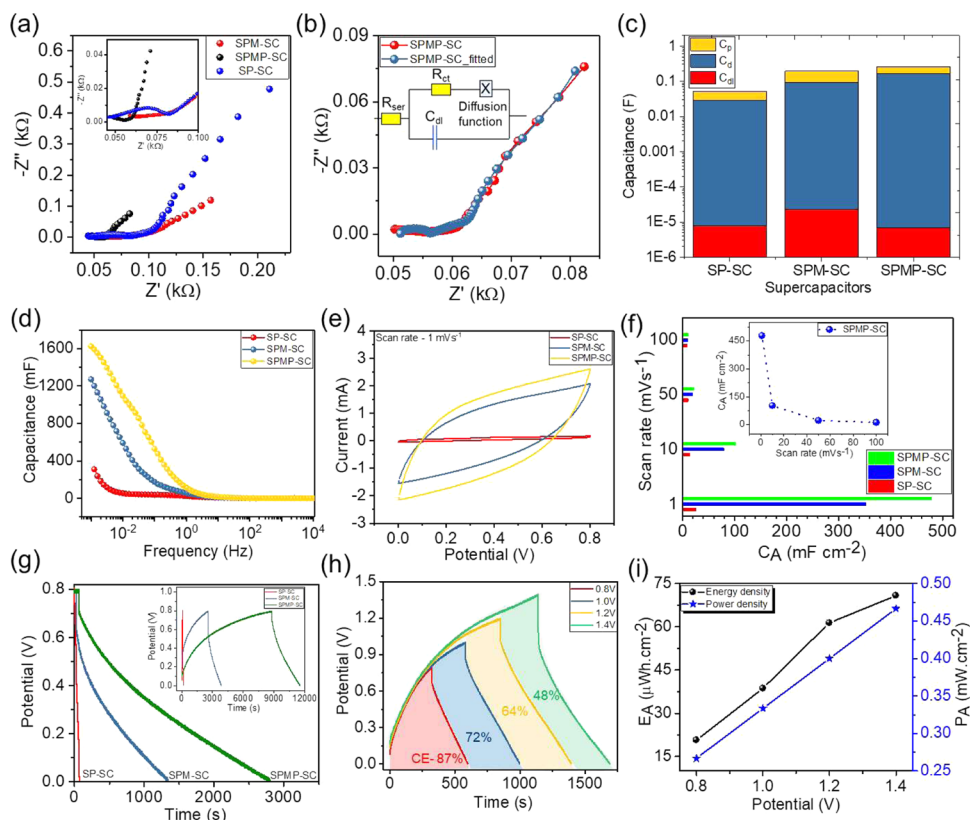
Figure 3. Electrochemical analysis of the SSCs. (a) Comparison of the Nyquist plot, with the inset showing the high-frequency region. (b) Electrochemical circuit fitting of the Nyquist plot of SPMP-SC;. (c) Comparison of various capacitances observed for the SSCs using fitting. (d) Variation of capacitance with frequencies of SSCs. (e) Comparison of CV spectra for the SSCs. (f) Comparison of the areal capacitances of the SCs measured from CV at various scan rates. The inset shows the decreasing capacitance for SPMP-SC. (g) Discharging curve of the SSCs at an applied current of 0.5 mA (inset shows the respective GCD curves). (h) Influence of operating potential on the GCD analysis of the SPMP-SC with Coulombic efficiency. (i) Ragone plot (obtained from the GCD analysis) showing the variation of the energy density and power density of the SPMP-SC.

are given in Table S1 in the Supporting Information. From the table, it can be observed that the lowest value of R_s is 53 Ω for SP-SC and it increased to 65 Ω with MnO_x deposition (SPM-SC) and then decreased to 51 Ω after 3D wrapping with PEDOT:PSS (SPMP-SC). Similarly, the value of R_{ct} decreased with 3D conductive wrapping of MnO_x with PEDOT:PSS. The fitting analysis shows that the total capacitance of the SC comprises the double-layer capacitance (C_{dl}), the diffusion capacitance (C_d), and the pseudocapacitance (C_p). The measured values of the capacitances for SP-SC, SPM-SC, and SPMP-SC are given in Table S1 in the Supporting Information. Figure 3c shows the comparison of capacitances of individual SCs. The high edlc value (C_{dl}) of MnO_x-based SC (SPM-SC), as compared to PEDOT:PSS, could be due to the highly porous and the NF morphology (shown in SEM image Figure 2h) of the MnO_x, which could lead to more ion interaction on the surface of the film through the faradic reaction. The electrochemical double-layer (edl) effect near the surface of the film leads to surface capacitance, denoted C_{dl}. In addition, the diffusion of ions from the electrolyte into the pores of the materials causes the generation of C_d due to ion insertion into the bulk phase of the material, and its value is higher for SPMP-SC (0.162 F). Due to diffusion of ions, the SPMP-SC shows the lowest values of R_{ct} (4.7 Ω) and R_s (51 Ω) given in Table S1, and hence, it leads to a high value of C_d. Moreover, we observed that the value of C_p (0.1 F for SPM-SC and 0.098 F for SPMP-SC) is prominent as compared to those of C_d and

C_{dl} for the SCs, and it could be due to the combined pseudocapacitance of the MnO_x and the conjugated polymer of the PEDOT:PSS. Further, we measured the total capacitance of the SC at different frequencies (expression given in the Supporting Information) as shown in Figure 3d. At the lowest frequency (1 mHz), the SP-SC has the lowest capacitance value of 310 mF and it increased to 1200 mF with MnO_x deposition (SPM-SC). This almost 4 times enhancement in capacitance is because of the highest pseudocapacitance contribution from the MnO_x NF. This value was further enhanced to 1600 mF after PEDOT:PSS (SPMP-SC) wrapping, thus confirming the 3D conductive network around the MnO_x NF to enhance the conductivity and thereby the capacitance.

The redox reaction that leads to the enhanced capacitance of the SPMP-SC was also confirmed by the cyclic voltammetry (CV) analysis, as shown in Figure 3e. The pseudo-rectangle curve represents the redox reaction of the metal oxides and conjugated polymers. Figure 3e shows a comparison of CV curves of SP-SC, SPM-SC, and SPMP-SC in the potential window of 0.8 V at a scan rate of 1 mV s^{-1}. The CV analysis, carried out in the scanning rate between 1 and 100 mV s^{-1} (shown in Figure S4a−c in the Supporting Information), shows that the acquired current of the SCs increases with increasing scanning rate (shown in Figure S5a,b). The almost linearly increasing current confirms the slow diffusion reaction as shown in the EIS analysis. The areal capacitance (C_A) values
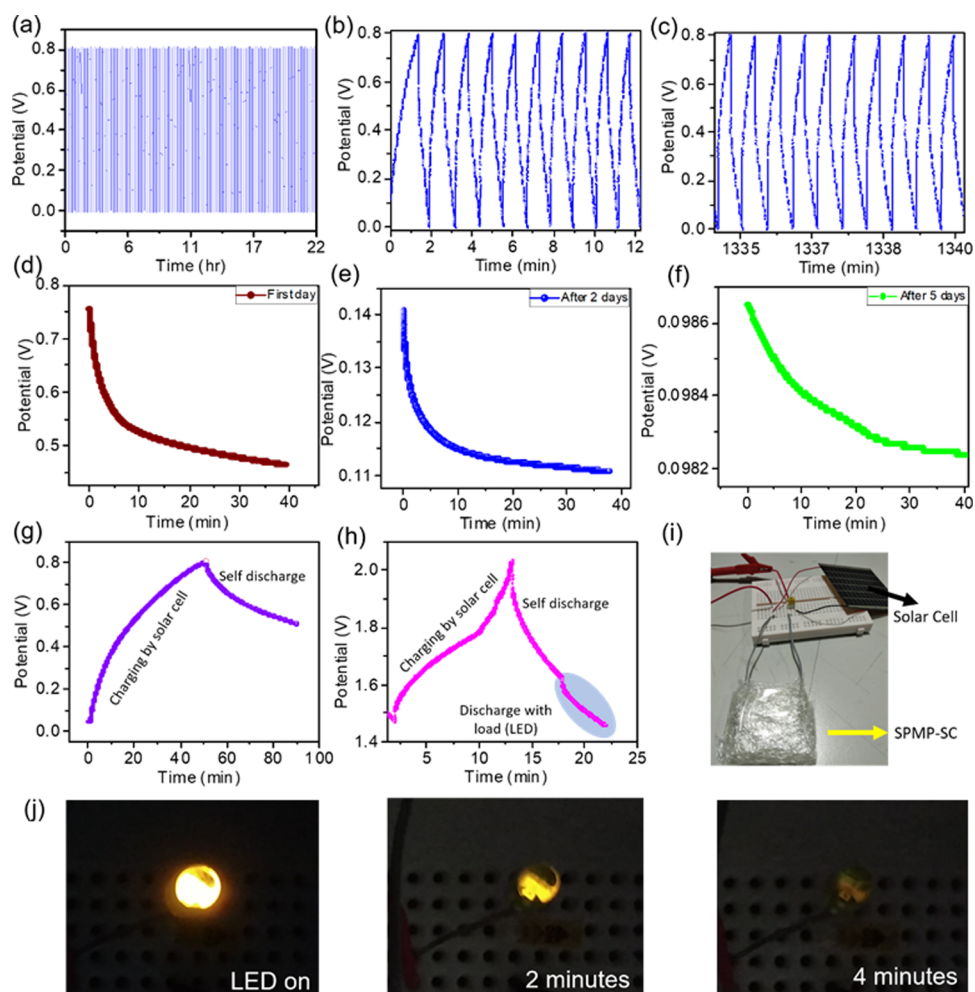
Figure 4. (a) SPMP-SC GCD curves at an applied current of 4 mA for 3000 cycles and (b, c) first and last 10 cycles of 3000 cycles, respectively. (d−f) Self-discharging of SPMP-SC on the 1st, 3rd, and 6th days. (g) Charging of SPMP-SC with the solar cell and self-discharge. (h) Charging of SPMP-SC with the solar cell and discharge with load (LED). (i) Photograph of SPMP-SC with the solar cell. (j) Lighting of an LED with SPMP-SC at different times.

of all three SSCs were calculated (expression given in the Supporting Information) from the CV curves at different scan rates, and the results are given in Figure 3f. The C_A of all three devices shows a decreasing trend with the scan rate. This is obvious as at a lower scanning rate, the diffusion of electrolyte ions into the inner pores of the electrode materials is higher and as a result the C_A is high. With increasing scanning rate, the diffusion of ions inside the materials decreases and eventually results in a lower specific capacitance. At a scan rate of 1 mV s^{-1}, the SP-SC shows the C_A of 26 mF·cm^{-2} (7.9 F·g^{-1}). In SP-SC, the pseudocapacitance from the PEDOT:PSS polymer as well as the edl formation is responsible for the observed capacitance. The C_A of SPM-SC was found to be 350 mF·cm^{-2} (75.4 F·g^{-1}), which is much higher in comparison with SP-SC. This is because, in addition to the contribution of PEDOT:PSS, the pseudocapacitance of both oxides (MnO_2 and Mn_3O_4) present in the deposited MnO_x film also contributed to the total capacitance of the device. The synergistic effect of both oxides in the MnO_x (MnO_2/Mn_3O_4) composite to the total capacitance is greater than that of the individual oxides.[43] The specific capacitance of SPMP-SC is even higher (479 mF·cm^{-2} (89.3 F·g^{-1})), owing to the combined effect of 3D wrapping of PEDOT:PSS on MnO_x, which reduces the contact resistance among the MnO_x

nanoparticles and also increases the underlying material access to the electrolyte ions.

The supercapacitive performances of the SSCs were investigated using galvanostatic charging−discharging (GCD) by applying current in the range of 0.5−1.0 mA, as shown in Figure S6. A comparison plot of the discharging curves for SP-SC, SPM-SC, and SPMP-SC, at an applied current of 0.5 mA, is given in Figure 3g (corresponding GCD curves are given in the inset). The specific capacitance obtained from the GCD plot (equation given in the Supporting Information) is the lowest (15 mF·cm^{-2} (4.7 F·g^{-1})) for SP-SC. Due to the presence of metal oxides, this value increases almost 18 times (275 mF·cm^{-2} (58.9 F·g^{-1})) for SPM-SC. The 3D wrapping further enhances the capacitance value for the SPMP-SC to 580 mF·cm^{-2} (108.1 F·g^{-1}). We also measured the areal energy density (E_A) for all three SSCs at an applied current of 0.5 mA, and these were found to be 1.4, 24.4, and 51.4 μWh·cm^{-2} for SP-SC, SPM-SC, and SPMP-SC, respectively. The significantly higher energy density of SPMP-SC shows that MnO_x deposition together with the 3D conductive wrapping resulted in a significant increase in the E_A value. The variation of E_A and C_A of all three devices with respect to CV and GCD analyses is given in Figure S7 in the Supporting Information. The influence of the operating potential on the SSC
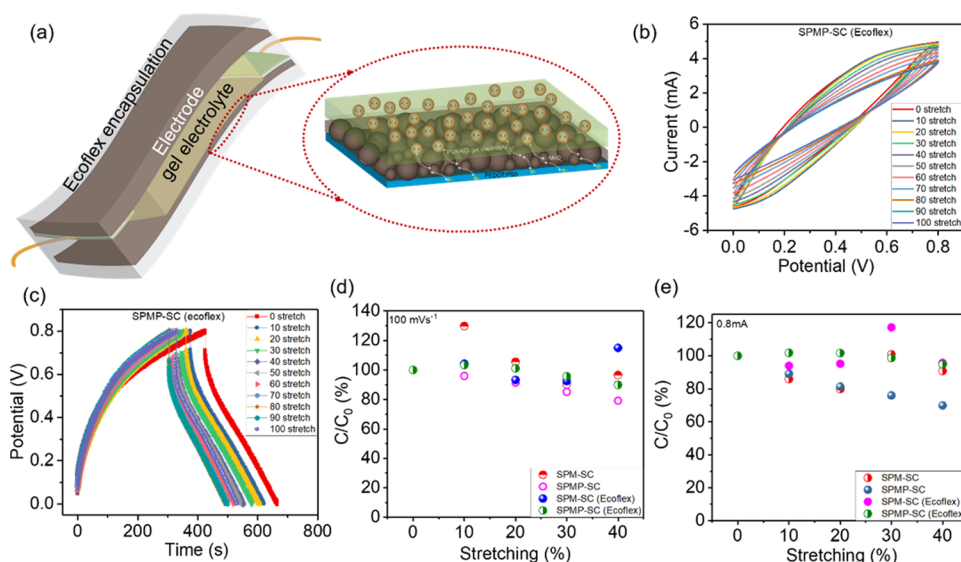
Figure 5. (a) Schematic of the stretchable SC with Ecoflex encapsulation and magnified schematics representing the ionic distribution for the charge-storing mechanism. (b, c) CV and GCD curves of SPMP-SCs with different stretchings. (d, e) Capacitance retention with stretching from CV (100 mV s^{-1}) and GCD analyses (0.8 mA), respectively.

performances and the Coulombic efficiency (CE) was also evaluated, and Figure 3h shows the GCD performances for SPMP-SC in the voltage range of 0.8−1.4 V with the respective CE values. We found that with an increasing operating potential window, the voltage drop (IR$_{drop}$) of the SC increased (given in Figure S8), which is similar to previously reported observations.[12] On the other hand, the CE value shows a decreasing trend with potential window. At 0.8 V, the SPMP-SC has the highest CE of 87%, and it decreased to 48% at a potential window of 1.4 V. This sharp decrease in the CE value is due to the high voltage drift that occurred at a higher potential. The Ragone plot for the SMP-SC for different operating potential windows is shown in Figure 3i, from where it may be noted that the energy and power densities increase on increasing the potential window. For many practical applications, high operating voltage and capacitance are needed to enhance the energy density of the SC. To achieve this, we integrated the fabricated SPMP-SC in series and parallel configurations. Figure S9a,b demonstrates the GCD performances of three SPMP-SC devices connected in series and parallel, and the measured energy and power density values are given in Table S2 in the Supporting Information.

The capacitance retention after cyclic GCD analysis was carried out for the SPMP-SC device with the applied current of 4 mA, and the results are shown in Figure 4a−c. Figure 4a shows the complete GCD curves of 3000 cycles, and Figure 4b,c indicates the first and last 10 cycles, respectively. The capacitance retention was calculated for each cycle, and the results showed 70% retention for 1000 cycles and 45% retention after 3000 cycles. Similarly, the self-discharge of SPMP-SC was also measured for 6 days, and the results are given in Figure 4d−f. As is evident from these figures, the device shows a low rate of self-discharge and maintained the potential around 0.1 V even after 5 days. These results indicate the better stability of the fabricated SSC against self-discharging. To demonstrate the potential of using the presented SPMP-SC for wearable applications, the device was charged with a flexible solar cell. Figure 4g depicts the charging of a single SPMP-SC device with a solar cell up to 0.8

V and its self-discharging after disconnecting the solar cell. Likewise, Figure 4h demonstrates the charging of three series-connected SPMP-SCs up to 2.0 V with the solar cell followed by self-discharging as well as discharging with a red LED. The photograph of the solar cell connection with the SC is given in Figure 4i. The charged SPMP-SCs (three devices connected in series) were then used to power an LED. As shown in Supplementary Video SV1 in the Supporting Information, the LED continued to glow for about 5 minutes, which indicates the excellent energy density of the SPMP-SC devices. Figure 4j shows the SPMP-SC-powered LED light at different time intervals.

3.4. Stretchability and Bendability Studies. The performance of the presented SSC under stretching and bending conditions was evaluated by encapsulating them in Ecoflex, as shown in Figures 1e and 5a. Figure 5b,c shows the CV and GCD curves of SPMP-SC with Ecoflex encapsulation under different stretching conditions (0−100%). We measured the capacitance retention of SPMP-SC and SPM-SC (from both CV and GCD analyses) with and without Ecoflex encapsulation (Figure S10 in the Supporting Information). There is an insignificant variation in the capacitance for stretching up to 40%, but after that, the SC shows an irreversible deformation. Figure 5d,e shows the capacitive retention of SPMP-SC and SPM-SC with and without Ecoflex encapsulation for CV and GCD analyses up to 40% stretching. This study reveals that the retention of capacitance is comparatively higher with Ecoflex encapsulation. This is because encapsulation prevents the electrolyte from drying and maintains a good ionic flow for a longer period.[59] As compared to SPM-SC, the SPMP-SC with Ecoflex encapsulation shows the highest capacitance retention of above 90%. This could also be due to the 3D wrapping of the polymer providing better interconnectivity for the electrode during stretching. A similar behavior is also observed in the cases of ESR (at 1 kHz) and IR$_{drop}$, as shown in Figure S11a,b in the Supporting Information. There was a sudden rise in IR$_{drop}$ and ΔESR values of SSC after 40% stretching due to the loss in contact within the conducting threads of the stretchable fabric.

Table 1. Comparison of Stretchable SC Performance[a]

electrode material	areal capacitance ($mF \cdot cm^{-2}$)	capacitance retention	encapsulation/substrate	ref
MnO_2-coated carbon nanotube fibers	33.75	nearly unchanged (100% strain and 20 stretching–releasing cycles)	no	59
polypyrrole@carbon nanotube yarn	67	nearly unchanged (80% strain)	urethane elastic fiber	60
carbon nanotube@MnO_2 fiber	65.32	nearly unchanged (20% strain)	no	61
PEDOT-modified textile	640[a]	81% after 2000 cycles	PDMS	62
biscrolled MnO_2/CNT yarn	889	nearly unchanged (30% strain)	no	63
polypyrrole-coated MnO_2 nanoparticles deposited on CNT textile	461[b]	98.5% (energy, 21% tensile strain) and no change (13% bending strain)	no	10
SPMP-SC	580 (0.5 mA)	90% (40% stretching and 1000 cycles)	Ecoflex	this work

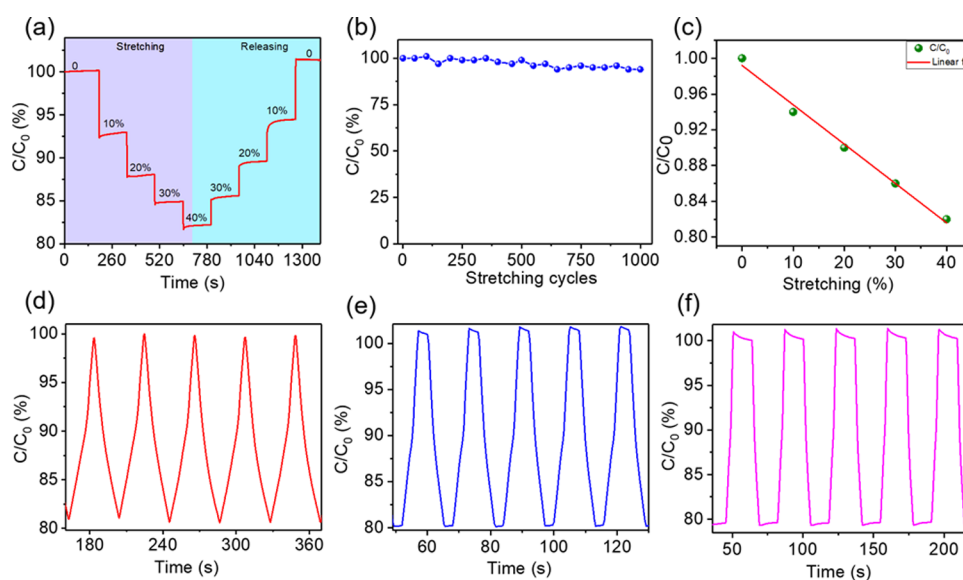[a]Three electrode. [b]$F \cdot g^{-1}$.

Figure 6. (a) Capacitance change during cyclic stretching and releasing of SPMP-SC (Ecoflex) up to 40% stretching. (b) Capacitance retention up to 1000 cycles of stretching. (c) Linear fitting of capacitance change with stretching. (d)−(f) Cyclic stability of capacitance variation with different holding times after stretching.

Similarly, the variation of the Coulombic efficiency retention with different strains was analyzed for SPMP-SCs (Figure S11c in the Supporting Information), and the results indicate a slight increase in efficiency at the initial stretching, and then, it remains almost constant (nearly 100%) for further stretching. Finally, the capacitance retention of this SSC was compared with reported textile-/fiber-based SC, and the results are shown in Table 1.[11,60−64]

The developed SSC shows a slightly better/comparable areal capacitance and capacitance retention compared to some of the reported works. Likewise, the capacitance retention against static bending deformations was also evaluated for all three SCs (SP-SC, SPM-SC, and SPMP-SC), and the results are given in Figure S12a (Supporting Information). The high capacitance retention (above 90%) for all of the devices suggests excellent device stability against mechanical deformations. The representative CV curves and the Nyquist plot of SPMP-SC are also given in Figure S11b,c (Supporting Information). Other than the stretchable gel electrolyte, the PVA can also be used as a self-healing material for encapsulation with proper modifications.[65]

3.5. SSC as a Strain Sensor. The stretchability analysis of the SPMP-SC shows an interesting phenomenon, i.e., the device has a linear variation in capacitance during stretching and releasing the strain. This linear variation in capacitance is supposed to be arising from the disconnection mechanism.[66,67] During stretching, 3D-wrapped conductive electrode materials loses the electrical contact with each other, which results in an increased ESR value and thereby a lower total capacitance.[68] However, this change is reversible for the applied strain values, and upon releasing the strain, the electrode reforms the interconnection and the SC regains the capacitance value. We also carried out the cyclic stability of the SC during stretching for SPMP-SC with Ecoflex encapsulation. Figure 6a shows the variation of relative capacitance (C/C_0) with different stretching and releasing strains (up to 40%) with a holding time of 60 seconds after each stretching. The results show a linear variation of capacitance with stretching, and the value remains the same while holding at each stretched condition. Interestingly, during the releasing cycle, the SSC regains its capacitance as that of stretching at the same strain (Supplementary Video SV2). This shows that the hysteresis of the SSC is negligible under different stretching conditions. The cyclic stability of retention of capacitance of this device was also measured for 1000 stretching and releasing cycles (in Figure 6b), and it gives a high capacitance retention of above 93%. These results represent a performance similar to that of a strain sensor, and hence, the presented SSC could also be used
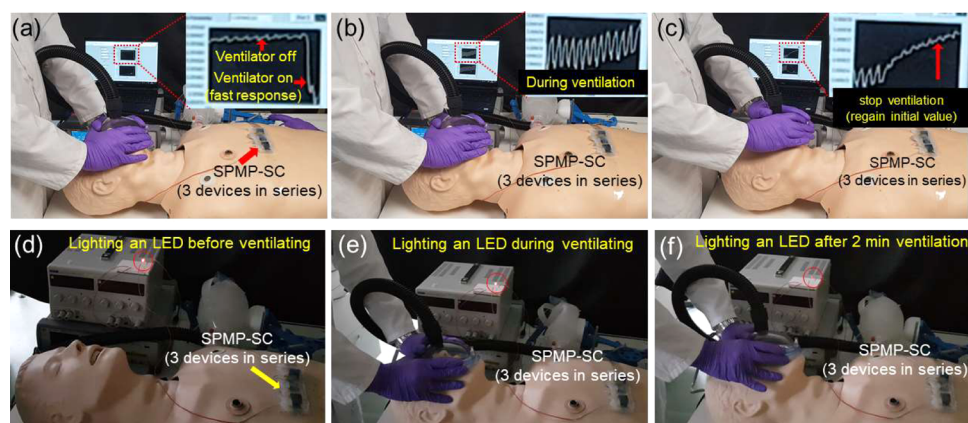
Figure 7. Dual function of the SPMP-SC (a−c) as an intrinsic strain sensor for monitoring the chest expansion during ventilation. (d−f) Constant power out of the SC during ventilation (stretching) by lighting an LED.

as a strain sensor, in addition to the conventional use as an energy/power storage device. To investigate further on these aspects, we analyzed the variation of capacitance with each strain, and the result is given in Figure 6c. A perfect linear fit of capacitance value with different stretching (strain) can be observed (with an R factor of 0.99 and a sensitivity of −0.4%) from Figure 6c. The sensitivity and high cyclic stability of SSC further ensure the intrinsic sensor performance of the device. Figure 6d−f shows the cyclic variation of the capacitance with different holding times after stretching. It is evident from these results that in different stretching and holding conditions the sensor performance of SSC is quite stable, which reaffirms the practical suitability of the developed device as an intrinsic strain-sensing supercapacitor for applications such as wearable energy storage or energy-autonomous eSkin for robots, as demonstrated in the next section.

3.6. Dual-Function Application of the SSC for Wearable Systems. The application of the developed SSC (SPMP-SC) as an intrinsic strain sensor as well as energy storage device is demonstrated in Figure 7. Figure 7a−c shows the strain-sensing performance of the SSC by capturing the volumetric expansion of the manikin's chest due to air supplied by a DIY ventilator, described elsewhere.[56] The demonstrated application resonates well with the current pandemic situation. As shown in Figure 7a, the SSC shows a stable capacitance before starting the ventilator and a sudden drop in capacitance when the ventilator is turned on. This rapid change in capacitance during stretching (i.e., chest expansion due to ventilation) indicates the fast response of the sensor on external stimuli. Similarly, in Figure 7b, the cyclic variation in the capacitance during ventilation (each inhale and exhale cycle) confirms the stability and repeatability of the sensor. This stable performance of the SSC as a sensor can also help in terms of real-time monitoring of vital signals (respiratory sensor), which have a greater importance in wearables for the healthcare sector. Finally, in Figure 7c, we show that the SSC regains its initial value once the ventilator is turned off (more details are given in Figure S13 and Video SV3). It is also important to demonstrate the constant powering ability of the SSC during this ventilation (stretching) operation to monitor the energy output for a connected device. To this end, we have also powered an LED using the SSCs and examined the change in the lighting condition during ventilation (Figure 7d−f). Figure 7d shows the glowing of the LED before starting the ventilation, and Figure 7e,f shows the lighting of the LED

during the beginning and after 2 min of ventilation. As is evident from these results, there is no appreciable change in the LED lighting during the stretching (ventilation) (Supporting Video SV4), which indicates an almost constant energy output of the SSC during its simultaneous operation as a strain sensor. Thus, we have also successfully demonstrated that the small change in the capacitance during the stretching of the SSC can be effectively utilized for sensor application. Further, to demonstrate the practical application of the SSC in robotics, the SPMP-SC was attached to the proximal interphalangeal joint (PIP) and the metacarpophalangeal joint of the index finger of a 3D-printed robotic hand and used as an angle feedback of the joints. The robotic hand was controlled via the Atmel AT91SAM3X8E microcontroller (μC). One of the microcontrollers' pulse width modulation (PWM) pin was connected to the servo motor, and external power sources were powering the system. More details about the hand design can be found in a previous work.[69] The servo motor attached to the finger was programmed to flex and relax the finger with a transition period of 0.5 s. The data were captured by an inductance−capacitance−resistance (LCR) unit. A custom-made LabView program was used to visualize and capture the data from the LCR system. The experimentation was done to validate the capability of the SPMP-SC as a feedback mechanism for robotic applications, and the result is shown in Supporting Video SV5.

4. CONCLUSIONS

In this work, we presented a stretchable fabric-based supercapacitor using lycra fabric (nylon and spandex mix) as the substrate and PEDOT:PSS as the current collector. The capacitance and energy density of the developed SSC were significantly improved by the electrochemical deposition of MnO_x NFs and 3D conductive wrapping with PEDOT:PSS. To study the role of MnO_x deposition and conductive wrapping, we fabricated three types of SSCs, namely, SP-SC (PEDOT:PSS), SPM-SC (PEDOT:PSS/MnO_x), and SPMP-SC (PEDOT:PSS/MnO_x/PEDOT:PSS). The microstructural investigations of all of the fabric electrodes were analyzed, and the SPMP-SC showed the best performance with a C_A of 580 mF cm^{-2} (108.1 F·g^{-1}) and an E_A of 51.4 μWh·cm^{-2} at an applied current of 0.5 mA. The capacitance retention of the SPMP-SC was calculated for each cycle, and the results showed a better retention of around 70% for 1000 cycles and 45% after 3000 cycles. Similarly, the capacitance retention of all of these

SCs with and without Ecoflex encapsulation at different stretching conditions was analyzed, and the SPMP-SC (Ecoflex encapsulation) showed a high capacitance retention above 90% upon 40% stretching up to 1000 cycles. The cyclic stability and linear variation of the capacitance change with stretching with an R value of 0.99 confirm the sensor performance of the fabricated SSC. Finally, the dual use of the presented SSC has been shown for potential applications in wearable systems and robotics.

■ ASSOCIATED CONTENT

ⓢ Supporting Information

The Supporting Information is available free of charge at https://pubs.acs.org/doi/10.1021/acsami.1c12526.

> Experimental details for electrodeposition of MnO_x on PEDOT:PSS-coated cloth (Figure S1); Bode plots of SSCs (Figure S2); electrochemical circuit fitting of the Nyquist plot of SP-SC and SPM-SC (Figure S3); fitting parameters of Nyquist plots (Table S1); CV curves of SP-SC, SPM-SC, and SPMP-SC at different scan rates (Figure S4); peak current with scanning rates of SP-SC, SPM-SC, and SPMP-SC (Figure S5); GCD curve of SPMP-SC at different applied currents (Figure S6); comparison of E_A and C_A from CV and GCD analyses of SSCs (Figure S7); IR $_{drop}$ with applied voltage (Figure S8); GCD curves of three SPMP-SCs in series and parallel connections (Figure S9); energy and power densities in series and parallel connections (Table S2); capacitance retention of SPMP-SC at 100% stretching (Figure S10); variation of ΔESR and ΔIR drop, (c) Coulombic efficiency of SPMP-SC at different stretchings (Figure S11); capacitance retention CV curves at 100 mV s^{-1} scan rate and Nyquist plot of SPMP-SC at different bending radii (Figure S12); SPMP-SC performance during ventilation (Figure S13); calculations (PDF)
>
> Powering an LED (MP4)
>
> Stretching analysis of SPMP-SC (MP4)
>
> Demo of SC as a wearable strain sensor on a manikin during ventilation (MP4)
>
> Lighting an LED during ventilator operation (MP4)
>
> Demo of SPMP-SC as a feedback system on a 3D-printed robotic hand attached to the proximal interphalangeal joint (PIP) and the metacarpophalangeal (MCP) (MP4)

■ AUTHOR INFORMATION

Corresponding Author

Ravinder Dahiya − *Bendable Electronics and Sensing Technologies (BEST) Group, School of Engineering, University of Glasgow, Glasgow G12 8QQ, U.K.;* ⓞ orcid.org/0000-0002-3858-3841; Phone: +44 (0) 141 330 5653; Email: Ravinder.Dahiya@glasgow.ac.uk

Authors

Abhilash Pullanchiyodan − *Bendable Electronics and Sensing Technologies (BEST) Group, School of Engineering, University of Glasgow, Glasgow G12 8QQ, U.K.*

Libu Manjakkal − *Bendable Electronics and Sensing Technologies (BEST) Group, School of Engineering, University of Glasgow, Glasgow G12 8QQ, U.K.;* ⓞ orcid.org/0000-0001-7933-6321

Markellos Ntagios − *Bendable Electronics and Sensing Technologies (BEST) Group, School of Engineering, University of Glasgow, Glasgow G12 8QQ, U.K.*

Complete contact information is available at:
https://pubs.acs.org/10.1021/acsami.1c12526

Author Contributions

The manuscript was written through contributions of all authors. All authors have given approval to the final version of the manuscript.

Notes

The authors declare no competing financial interest.

■ ACKNOWLEDGMENTS

■ REFERENCES

(1) Lipomi, D. J.; Vosgueritchian, M.; Tee, B. C. K.; Hellstrom, S. L.; Lee, J. A.; Fox, C. H.; Bao, Z. Skin-like Pressure and Strain Sensors Based on Transparent Elastic Films of Carbon Nanotubes. *Nat. Nanotechnol.* **2011**, *6*, 788−792.

(2) Wang, X.; Liu, Z.; Zhang, T. Flexible Sensing Electronics for Wearable/Attachable Health Monitoring. *Small* **2017**, *13*, No. 1602790.

(3) Kim, D.; Kim, D.; Lee, H.; Jeong, Y. R.; Lee, S. J.; Yang, G.; Kim, H.; Lee, G.; Jeon, S.; Zi, G.; Kim, J.; Ha, J. S. Body-Attachable and Stretchable Multisensors Integrated with Wirelessly Rechargeable Energy Storage Devices. *Adv. Mater.* **2016**, *28*, 748−756.

(4) Núñez, C. G.; Navaraj, W. T.; Polat, E. O.; Dahiya, R. Energy-Autonomous, Flexible, and Transparent Tactile Skin. *Adv. Funct. Mater.* **2017**, *27*, No. 1606287.

(5) Huang, Y.; Zhong, M.; Shi, F.; Liu, X.; Tang, Z.; Wang, Y.; Huang, Y.; Hou, H.; Xie, X.; Zhi, C. An Intrinsically Stretchable and Compressible Supercapacitor Containing a Polyacrylamide Hydrogel Electrolyte. *Angew. Chem., Int. Ed.* **2017**, *56*, 9141−9145.

(6) Wang, L.; Lou, Z.; Jiang, K.; Shen, G. Bio-Multifunctional Smart Wearable Sensors for Medical Devices. *Adv. Intell. Syst.* **2019**, *1*, No. 1900040.

(7) Koydemir, H. C.; Ozcan, A. Wearable and Implantable Sensors for Biomedical Applications. *Annu. Rev. Anal. Chem.* **2018**, 127−146.

(8) Datta, R. S.; Syed, N.; Zavabeti, A.; Jannat, A.; Mohiuddin, M.; Rokunuzzaman, M.; Yue Zhang, B.; Rahman, M. A.; Atkin, P.; Messalea, K. A.; Ghasemian, M. B. Flexible Two-Dimensional Indium Tin Oxide Fabricated Using a Liquid Metal Printing Technique. *Nat. Electron.* **2020**, *3*, 51−58.

(9) Dang, W.; Manjakkal, L.; Navaraj, W. T.; Lorenzelli, L.; Vinciguerra, V.; Dahiya, R. Stretchable Wireless System for Sweat PH Monitoring. *Biosens. Bioelectron.* **2018**, *107*, 192−202.

(10) Manjakkal, L.; Dang, W.; Yogeswaran, N.; Dahiya, R. Textile-Based Potentiometric Electrochemical pH Sensor for Wearable Applications. *Biosensors* **2019**, *9*, 14.

(11) Yun, T. G.; Hwang, B.; Kim, D.; Hyun, S.; Han, S. M. Polypyrrole-MnO$_2$-Coated Textile-Based Flexible-Stretchable Supercapacitor with High Electrochemical and Mechanical Reliability. *ACS Appl. Mater. Interfaces* **2015**, *7*, 9228−9234.

(12) Manjakkal, L.; Pullanchiyodan, A.; Yogeswaran, N.; Hosseini, E. S.; Dahiya, R. A Wearable Supercapacitor Based on Conductive PEDOT:PSS-Coated Cloth and a Sweat Electrolyte. *Adv. Mater.* **2020**, *32*, No. 1907254.

(13) Pullanchiyodan, A.; Manjakkal, L.; Dervin, S.; Shakthivel, D.; Dahiya, R. Metal Coated Conductive Fabrics with Graphite

Electrodes and Biocompatible Gel Electrolyte for Wearable Supercapacitors. *Adv. Mater. Technol.* **2020**, *5*, No. 1901107.

(14) Manjakkal, L.; Navaraj, W. T.; Núñez, C. G.; Dahiya, R. Graphene−Graphite Polyurethane Composite Based High-Energy Density Flexible Supercapacitors. *Adv. Sci.* **2019**, *6*, No. 1802251.

(15) An, T.; Cheng, W. Recent Progress in Stretchable Supercapacitors. *J. Mater. Chem. A.* **2018**, 15478−15494.

(16) Manjakkal, L.; Núñez, C. G.; Dang, W.; Dahiya, R. Flexible Self-Charging Supercapacitor Based on Graphene-Ag-3D Graphene Foam Electrodes. *Nano Energy* **2018**, *51*, 604−612.

(17) Soni, M.; Dahiya, R. Soft Eskin: Distributed Touch Sensing with Harmonized Energy and Computing. *Philos. Trans. R. Soc., A* **2020**, *378*, No. 20190156.

(18) Dahiya, R.; Yogeswaran, N.; Liu, F.; Manjakkal, L.; Burdet, E.; Hayward, V.; Jorntell, H. Large-Area Soft e-Skin: The Challenges beyond Sensor Designs. *Proc. IEEE* **2019**, *107*, 2016−2033.

(19) Escobedo, P.; Ntagios, M.; Shakthivel, D.; Navaraj, W. T.; Dahiya, R. Energy Generating Electronic Skin with Intrinsic Tactile Sensing without Touch Sensors. *IEEE Trans. Robot.* **2021**, *37*, 683−690.

(20) Ozioko, O.; Karipoth, P.; Escobedo, P.; Ntagios, M.; Pullanchiyodan, A.; Dahiya, R. SensAct: The Soft and Squishy Tactile Sensor with Integrated Flexible Actuator. *Adv. Intell. Syst.* **2021**, *3*, No. 1900145.

(21) Bhattacharjee, M.; Nikbakhtnasrabadi, F.; Dahiya, R. Printed Chipless Antenna as Flexible Temperature Sensor. *IEEE Internet Things J.* **2021**, *8*, 5101−5110.

(22) Zhang, Y.; Sezen, S.; Ahmadi, M.; Cheng, X.; Rajamani, R. Paper-Based Supercapacitive Mechanical Sensors. *Sci. Rep.* **2018**, *8*, No. 16284.

(23) Zhang, Y.; Sezen, S.; Cheng, X.; Rajamani, R. Supercapacitive Strain Sensor With Ultrahigh Sensitivity and Range. *IEEE Sens. Lett.* **2019**, *3*, No. 2500504.

(24) Rahim, M. A.; Centurion, F.; Han, J.; Abbasi, R.; Mayyas, M.; Sun, J.; Christoe, M. J.; Esrafilzadeh, D.; Allioux, F. M.; Ghasemian, M. B.; Yang, J.; Tang, J.; Daeneke, T.; Mettu, S.; Zhang, J.; Uddin, M. H.; Jalili, R.; Kalantar-Zadeh, K. Polyphenol-Induced Adhesive Liquid Metal Inks for Substrate-Independent Direct Pen Writing. *Adv. Funct. Mater.* **2021**, *31*, No. 2007336.

(25) Yang, J.; Cheng, W.; Kalantar-Zadeh, K. Electronic Skins Based on Liquid Metals. *Proc. IEEE.* **2019**, 2168−2184.

(26) Yuksel, R.; Unalan, H. E. Textile Supercapacitors-Based on MnO_2/SWNT/Conducting Polymer Ternary Composites. *Int. J. Energy Res.* **2015**, *39*, 2042−2052.

(27) Zhang, Q.; Sun, J.; Pan, Z.; Zhang, J.; Zhao, J.; Wang, X.; Zhang, C.; Yao, Y.; Lu, W.; Li, Q.; Zhang, Y.; Zhang, Z. Stretchable Fiber-Shaped Asymmetric Supercapacitors with Ultrahigh Energy Density. *Nano Energy* **2017**, *39*, 219−228.

(28) Jost, K.; Dion, G.; Gogotsi, Y. Textile Energy Storage in Perspective. *J. Mater. Chem. A.* **2014**, 10776−10787.

(29) Zhai, S.; Karahan, H. E.; Wei, L.; Qian, Q.; Harris, A. T.; Minett, A. I.; Ramakrishna, S.; Ng, A. K.; Chen, Y. Textile Energy Storage: Structural Design Concepts, Material Selection and Future Perspectives. *Energy Storage Mater.* **2016**, 123−139.

(30) Hu, L.; Chen, W.; Xie, X.; Liu, N.; Yang, Y.; Wu, H.; Yao, Y.; Pasta, M.; Alshareef, H. N.; Cui, Y. Symmetrical MnO_2-Carbon Nanotube-Textile Nanostructures for Wearable Pseudocapacitors with High Mass Loading. *ACS Nano* **2011**, *5*, 8904−8913.

(31) He, S.; Hu, C.; Hou, H.; Chen, W. Ultrathin MnO_2 Nanosheets Supported on Cellulose Based Carbon Papers for High-Power Supercapacitors. *J. Power Sources* **2014**, *246*, 754−761.

(32) Hu, Z.; Xiao, X.; Chen, C.; Li, T.; Huang, L.; Zhang, C.; Su, J.; Miao, L.; Jiang, J.; Zhang, Y.; Zhou, J. Al-Doped α-MnO_2 for High Mass-Loading Pseudocapacitor with Excellent Cycling Stability. *Nano Energy* **2015**, *11*, 226−234.

(33) Huang, G.; Zhang, Y.; Wang, L.; Sheng, P.; Peng, H. Fiber-Based MnO_2/Carbon Nanotube/Polyimide Asymmetric Supercapacitor. *Carbon* **2017**, *125*, 595−604.

(34) Huang, M.; Li, F.; Dong, F.; Zhang, Y. X.; Zhang, L. L. MnO_2-Based Nanostructures for High-Performance Supercapacitors. *J. Mater. Chem. A.,* **2015**, 21380−21423.

(35) Kim, J. H.; Choi, C.; Lee, J. M.; de Andrade, M. J.; Baughman, R. H.; Kim, S. J. Ag/$MnO2$ Composite Sheath-Core Structured Yarn Supercapacitors. *Sci. Rep.* **2018**, *8*, No. 13309.

(36) Li, W.; Xu, K.; Li, B.; Sun, J.; Jiang, F.; Yu, Z.; Zou, R.; Chen, Z.; Hu, J. MnO_2 Nanoflower Arrays with High Rate Capability for Flexible Supercapacitors. *ChemElectroChem* **2014**, *1*, 1003−1008.

(37) Shi, J.; Sun, M.; Hu, H. One-Step Combustion Synthesis of C-Mn_3O_4/MnO Composites with High Electrochemical Performance for Supercapacitor. *Mater. Res. Express* **2019**, *6*, No. 035511.

(38) Sambath Kumar, K.; Cherusseri, J.; Thomas, J. Two-Dimensional Mn_3O_4 Nanowalls Grown on Carbon Fibers as Electrodes for Flexible Supercapacitors. *ACS Omega* **2019**, *4*, 4472−4480.

(39) Wang, L.; Chen, L.; Li, Y.; Ji, H.; Yang, G. Preparation of Mn_3O_4 Nanoparticles at Room Condition for Supercapacitor Application. *Powder Technol.* **2013**, *235*, 76−81.

(40) Suktha, P.; Phattharasupakun, N.; Dittanet, P.; Sawangphruk, M. Charge Storage Mechanisms of Electrospun Mn_3O_4 Nanofibres for High-Performance Supercapacitors. *RSC Adv.* **2017**, *7*, 9958−9963.

(41) Dong, R.; Ye, Q.; Kuang, L.; Lu, X.; Zhang, Y.; Zhang, X.; Tan, G.; Wen, Y.; Wang, F. Enhanced Supercapacitor Performance of Mn_3O_4 Nanocrystals by Doping Transition-Metal Ions. *ACS Appl. Mater. Interfaces* **2013**, *5*, 9508−9516.

(42) Li, D.; Meng, F.; Yan, X.; Yang, L.; Heng, H.; Zhu, Y. One-Pot Hydrothermal Synthesis of Mn_3O_4 Nanorods Grown on Ni Foam for High Performance Supercapacitor Applications. *Nanoscale Res. Lett.* **2013**, *8*, No. 535.

(43) Wu, T. H.; Hesp, D.; Dhanak, V.; Collins, C.; Braga, F.; Hardwick, L. J.; Hu, C. C. Charge Storage Mechanism of Activated Manganese Oxide Composites for Pseudocapacitors. *J. Mater. Chem. A* **2015**, *3*, 12786−12795.

(44) Yu, G.; Hu, L.; Liu, N.; Wang, H.; Vosgueritchian, M.; Yang, Y.; Cui, Y.; Bao, Z. Enhancing the Supercapacitor Performance of Graphene/MnO_2 Nanostructured Electrodes by Conductive Wrapping. *Nano Lett.* **2011**, *11*, 4438−4442.

(45) Huang, Y.; Huang, Y.; Meng, W.; Zhu, M.; Xue, H.; Lee, C. S.; Zhi, C. Enhanced Tolerance to Stretch-Induced Performance Degradation of Stretchable MnO_2-Based Supercapacitors. *ACS Appl. Mater. Interfaces* **2015**, *7*, 2569−2574.

(46) Wang, J.-G. Engineering Nanostructured MnO_2 for High Performance Supercapacitors. In *Supercapacitor Design and Applications*; InTech, 2016.

(47) Lu, X.; Zhai, T.; Zhang, X.; Shen, Y.; Yuan, L.; Hu, B.; Gong, L.; Chen, J.; Gao, Y.; Zhou, J.; Tong, Y.; Wang, Z. L. WO_{3-X}@Au@MnO_2 Core-Shell Nanowires on Carbon Fabric for High-Performance Flexible Supercapacitors. *Adv. Mater.* **2012**, *24*, 938−944.

(48) Sadak, O.; Wang, W.; Guan, J.; Sundramoorthy, A. K.; Gunasekaran, S. MnO_2 Nanoflowers Deposited on Graphene Paper as Electrode Materials for Supercapacitors. *ACS Appl. Nano Mater.* **2019**, *2*, 4386−4394.

(49) Su, Z.; Yang, C.; Xu, C.; Wu, H.; Zhang, Z.; Liu, T.; Zhang, C.; Yang, Q.; Li, B.; Kang, F. Co-Electro-Deposition of the MnO_2-PEDOT:PSS Nanostructured Composite for High Areal Mass, Flexible Asymmetric Supercapacitor Devices. *J. Mater. Chem. A.,* **2013**, *1*, 12432−12440.

(50) Hou, Y.; Cheng, Y.; Hobson, T.; Liu, J. Design and Synthesis of Hierarchical MnO_2 Nanospheres/Carbon Nanotubes/Conducting Polymer Ternary Composite for High Performance Electrochemical Electrodes. *Nano Lett.* **2010**, *10*, 2727−2733.

(51) Chen, S.; Zhu, J.; Wu, X.; Han, Q.; Wang, X. Graphene Oxide-Mno2 Nanocomposites for Supercapacitors. *ACS Nano* **2010**, *4*, 2822−2830.

(52) Wu, Z. S.; Ren, W.; Wang, D. W.; Li, F.; Liu, B.; Cheng, H. M. High-Energy MnO_2 Nanowire/Graphene and Graphene Asymmetric Electrochemical Capacitors. *ACS Nano* **2010**, *4*, 5835−5842.

(53) Wang, J. G.; Yang, Y.; Huang, Z. H.; Kang, F. Coaxial Carbon Nanofibers/MnO$_2$ Nanocomposites as Freestanding Electrodes for High-Performance Electrochemical Capacitors. *Electrochim. Acta* **2011**, *56*, 9240−9247.

(54) Liu, R.; Sang, B. L. MnO$_2$/Poly(3,4-Ethylenedioxythiophene) Coaxial Nanowires by One-Step Coelectrodeposition for Electrochemical Energy Storage. *J. Am. Chem. Soc.,* **2008**, *130*, 2942−2943.

(55) Liu, F. J. Electrodeposition of Manganese Dioxide in Three-Dimensional Poly(3,4-Ethylenedioxythiophene)-Poly(Styrene Sulfonic Acid)-Polyaniline for Supercapacitor. *J. Power Sources* **2008**, *182*, 383−388.

(56) Christou, A.; Ntagios, M.; Hart, A.; Dahiya, R. GlasVent—The Rapidly Deployable Emergency Ventilator. *Glob. Challenges* **2020**, *4*, No. 2000046.

(57) Samuel, E.; Joshi, B.; Kim, Y.; Aldalbahi, A.; Rahaman, M.; Yoon, S. S. ZnO/MnO$_x$ Nanoflowers for High-Performance Supercapacitor Electrodes. *ACS Sustainable Chem. Eng.* **2020**, *8*, 3697−3708.

(58) Singha, S. S.; Rudra, S.; Mondal, S.; Pradhan, M.; Nayak, A. K.; Satpati, B.; Pal, P.; Das, K.; Singha, A. Mn Incorporated MoS$_2$ Nanoflowers: A High Performance Electrode Material for Symmetric Supercapacitor. *Electrochim. Acta* **2020**, *338*, No. 135815.

(59) Thekkekara, L. V.; Gu, M. Large-Scale Waterproof and Stretchable Textile-Integrated Laser- Printed Graphene Energy Storages. *Sci. Rep.* **2019**, *9*, No. 11822.

(60) Xu, P.; Wei, B.; Cao, Z.; Zheng, J.; Gong, K.; Li, F.; Yu, J.; Li, Q.; Lu, W.; Byun, J. H.; Kim, B. S.; Yan, Y.; Chou, T. W. Stretchable Wire-Shaped Asymmetric Supercapacitors Based on Pristine and MnO$_2$ Coated Carbon Nanotube Fibers. *ACS Nano* **2015**, *9*, 6088−6096.

(61) Sun, J.; Huang, Y.; Fu, C.; Wang, Z.; Huang, Y.; Zhu, M.; Zhi, C.; Hu, H. High-Performance Stretchable Yarn Supercapacitor Based on PPy@CNTs@urethane Elastic Fiber Core Spun Yarn. *Nano Energy* **2016**, *27*, 230−237.

(62) Yu, J.; Lu, W.; Smith, J. P.; Booksh, K. S.; Meng, L.; Huang, Y.; Li, Q.; Byun, J. H.; Oh, Y.; Yan, Y.; Chou, T. W. A High Performance Stretchable Asymmetric Fiber-Shaped Supercapacitor with a Core-Sheath Helical Structure. *Adv. Energy Mater.* **2017**, *7*, No. 1600976.

(63) Yu, X.; Su, X.; Yan, K.; Hu, H.; Peng, M.; Cai, X.; Zou, D. Stretchable, Conductive, and Stable PEDOT-Modified Textiles through a Novel In Situ Polymerization Process for Stretchable Supercapacitors. *Adv. Mater. Technol.* **2016**, *1*, No. 1600009.

(64) Choi, C.; Kim, K. M.; Kim, K. J.; Lepró, X.; Spinks, G. M.; Baughman, R. H.; Kim, S. J. Improvement of System Capacitance via Weavable Superelastic Biscrolled Yarn Supercapacitors. *Nat. Commun.* **2016**, *7*, No. 13811.

(65) Merhebi, S.; Mayyas, M.; Abbasi, R.; Christoe, M. J.; Han, J.; Tang, J.; Rahim, M. A.; Yang, J.; Tan, T. T.; Chu, D.; Zhang, J.; Li, S.; Wang, C. H.; Kalantar-Zadeh, K.; Allioux, F. M. Magnetic and Conductive Liquid Metal Gels. *ACS Appl. Mater. Interfaces* **2020**, *12*, 20119−20128.

(66) Xu, H.; Lv, Y.; Qiu, D.; Zhou, Y.; Zeng, H.; Chu, Y. An Ultra-Stretchable, Highly Sensitive and Biocompatible Capacitive Strain Sensor from an Ionic Nanocomposite for on-Skin Monitoring. *Nanoscale* **2019**, *11*, 1570−1578.

(67) Amjadi, M.; Kyung, K. U.; Park, I.; Sitti, M. Stretchable, Skin-Mountable, and Wearable Strain Sensors and Their Potential Applications: A Review. *Adv. Funct. Mater.* **2016**, *26*, 1678−1698.

(68) Chen, F.; Chen, Q.; Song, Q.; Lu, H.; Ma, M. Strong and Stretchable Polypyrrole Hydrogels with Biphase Microstructure as Electrodes for Substrate-Free Stretchable Supercapacitors. *Adv. Mater. Interfaces* **2019**, *6*, No. 1900133.

(69) Ntagios, M.; Nassar, H.; Pullanchiyodan, A.; Navaraj, W. T.; Dahiya, R. Robotic Hands with Intrinsic Tactile Sensing via 3D Printed Soft Pressure Sensors. *Adv. Intell. Syst.* **2020**, *2*, No. 1900080.